LA-6173-MS
Informal Report

UC-20
Reporting Date: December 1975
Issued: December 1975

Design of the ZT-1 Toroidal Pinch Experiment

by

D. A. Baker
L. C. Burkhardt
R. S. Dike
J. N. Di Marco
P. R. Forman
A. Haberstich
H. J. Karr
L. W. Mann
J. A. Phillips*
A. E. Schofield

*Director of Physics Division, International Atomic Energy Agency, Headquarters, Vienna, Austria.

los alamos
scientific laboratory
of the University of California
LOS ALAMOS, NEW MEXICO 87545

An Affirmative Action/Equal Opportunity Employer

UNITED STATES
ENERGY RESEARCH AND DEVELOPMENT ADMINISTRATION
CONTRACT W-7405-ENG. 36

In the interest of prompt distribution, this report was not edited by the Technical Information staff.

Printed in the United States of America. Available from
National Technical Information Service
U.S. Department of Commerce
5285 Port Royal Road
Springfield, VA 22151
Price: Printed Copy $4.50 Microfiche $2.25

DESIGN OF THE ZT-1 TOROIDAL PINCH EXPERIMENT

by

D. A. Baker, L. C. Burkhardt, R. S. Dike, J. N. Di Marco, P. R. Forman,

A. Haberstich, H. J. Karr, L. W. Mann, J. A. Phillips, and A. E. Schofield

ABSTRACT

Electrical design details are given for a toroidal Z-pinch device named ZT-1 that uses field programming to achieve a stable, reversed field pinch. The plasma is formed in a 4-mm-thick, 10.3-cm-i.d., high-alumina, segmented ceramic vacuum chamber. Voltages as high as 70 kV are routinely attained by interrupting with a fuse 800 kA in an inductive store. The current is diverted from the fuse to the primary of a single-turn transformer divided into quadrants. A total of 280 kV at 200 kA can then be applied to the plasma, which forms the secondary circuit of the transformer. This system produces dB_θ/dt's of up to 8 T/μs; with modifications to the electrical system, dB_θ/dt's as low as 0.1 T/μs are obtained. The B_z bias field of up to 0.25 T can be reversed at a rate of up to 0.2 T/μs. Both B_θ and B_z magnetic field errors are minimized. The design of the fuses and magnetic core and the development of a low inductance and resistance metal-to-metal crowbar are described.

I. INTRODUCTION

Although the early Z-pinch results were characterized by short, stable lifetimes and ion temperatures of $\gtrsim$ 100 eV, several recent experiments have obtained significantly longer stable times and higher temperatures. Ohkawa et al.[1] obtained improved performance in a toroidal Z-pinch experiment by programming magnetic fields and reducing magnetic field errors. Robinson and King[2] report a prolonged stable period limited by classical diffusion of fields for a diffuse Z pinch. Bobeldijk et al.[3] and Wilhelm and Zwicker[4] report lifetimes up to 20 μs, also limited by field diffusion, and temperatures up to 1000 eV for screw-pinch experiments. Di Marco and Burkhardt[5] have obtained ion temperatures of $\sim$ 500 eV and containment times of $\sim$ 10 μs limited by end effects in a linear Z pinch.

Numerical calculations of implosion heating[6] predict plasma temperatures of several keV for both Θ and Z pinches for comparable starting conditions using field magnitudes readily available in the laboratory. However, in past experiments, Z pinches have not attained temperatures as high as those observed with the Θ pinch. This can be attributed to differences in starting conditions. An important parameter in the implosion-heating process is the initial rate of rise of the magnetic "piston" driving the plasma.[7] Using the snowplow model, it can be shown[8] that the initial acceleration is proportional to $(dB/dt)/\sqrt{\rho}$ where dB/dt is the rate of change of magnetic field at the plasma surface and ρ is the initial plasma density. Compared to the Θ pinches, past Z-pinch experiments did not achieve comparable $\dot{B}/\sqrt{\rho}$ with two exceptions. The first[9] employed a discharge volume 1 cm in diameter and 2 cm long, limiting diagnostics severely. The second[10] experienced secondary wall breakdown after pinch formation.

The ZT-1 toroidal Z-pinch experiment employs a magnetic energy storage system and fuse switching to extend the range of the Z-pinch experiment. This affords a high-voltage source capable of supplying current at a rate of $\sim 2 \times 10^{12}$ A/s with peak discharge voltages of $\sim$ 70 kV per torus quadrant and

peak currents of $\gtrsim$ 200 kA. With these short current and voltage risetimes, the value of $\dot{B}\sqrt{\rho}$ exceeds those attained with present θ pinches. The voltage rises to its peak value in ∿ 0.3 μs, then falls to a low value in $\lesssim$ 2 μs to avoid secondary wall breakdown problems.

In this report, the design and operation of the ZT-1 system are described. The torus assembly and the magnetic energy storage system are discussed in Sec. II and the field programming and associated electronic circuitry in Sec. III. In Sec. IV, the theory of the fuse switching and inductive storage behavior is reviewed with results of the analog field and current flow mapping used in the system design. The measures taken for correction of magnetic field errors are given in Sec. V. The iron core design and testing procedure are described in Sec. VI. Spark gap and crowbar test results are given in Sec. VII.

II. TORUS ASSEMBLY AND MAGNETIC ENERGY STORAGE SYSTEM

Figures 1 and 2 are isometric sectional drawings of the ZT-1 system. The requirement of very high current rise (∿ 2 x 10^{12} A/s) for the implosion heating has been attained by high-voltage, low-inductance design and a unique magnetic energy storage and fuse switching system. The toroidal discharge tube is located within a large coaxial "barrel" 244 cm in diameter and 90 cm high. The barrel is made from 1.87-cm-thick aluminum with reinforcing ribs to withstand the large magnetic forces. There is 0.15-cm total thickness of layered mylar insulation between the coaxial cylinders of the barrel. This insulation has been tested conservatively at ∿ 100 kV. The function of the barrel is to act as a magnetic energy storage inductor symmetrically connected to the coaxial cables from the capacitor bank at the bottom end, and also symmetrically connected to the four fuses and parallel-plate transmission lines to the torus at the upper end. The storage inductor is formed near the bottom of the barrel by reducing the radius of the inner coaxial conductor over an axial length of ∿ 50 cm. An array of vertical bars, shown in Fig. 1, forms the inner conductor of this section and is moveable to allow the radius and, thereby, the storage inductance to be varied from 5 to 40 nH.

The top of the barrel is contoured to connect with the four tapered parallel-plate transmission lines. These lines connect in turn to the four fuses, transfer switches, and the four feedpoints of the torus primary. When the capacitor bank spark gap switches (see Sec. III) are triggered, current flows through the barrel, a section of the parallel plate lines, and the four fuses. As the current rises, magnetic energy is stored in the inductor. After ∿ 7 μs, the resistance of the fuses increases by a factor of ∿ 100 as they vaporize, and, due to the circuit inductance, voltages ∿ 5 times the bank voltage are developed across the fuses. The rise in voltage causes the transfer spark gap switches to fire transferring the voltage and current to the torus. The voltage across each fuse drives one-quarter section of the toroidal discharge. A voltage as high as 80 kV per quadrant can be developed with the present system. However, to avoid possible insulation breakdown, 60 to 70 kV have been chosen. This technique affords very rapid transfer of current to the pinch discharge because of the high voltage and low load inductance. A more detailed and quantitative analysis of the magnetic energy storage and fuse switching circuit behavior is given in Sec. IV.

Simultaneous operation of the fuses and transfer switches in the four quadrants is essential to produce the same voltage and current characteristics at the four feedpoints in the torus. In the event of mismatch in fuse operation, current from adjacent fuses will be diverted to the one having lower voltage because of the coupling between fuses by the contoured sections of the barrel. Questions of simultaneity and jitter are considered in more detail in Sec. IV.

The torus primary, also shown in Fig. 1, is made of 1.27-cm wall thickness, 11.6-cm bore, aluminum. The mean major diameter is 76 cm. This primary is assembled in four sections and is split in the meridian plane for ease of assembly and to provide an insulated gap around the inner major circumference. This inner gap allows rapid penetration of the toroidal magnetic field into the torus. There is a toroidal winding of 66 turns of #8 wire around each quadrant of the aluminum primary with the current return through the primary to minimize field errors. The maximum $\dot{B}_z$ is obtained with two

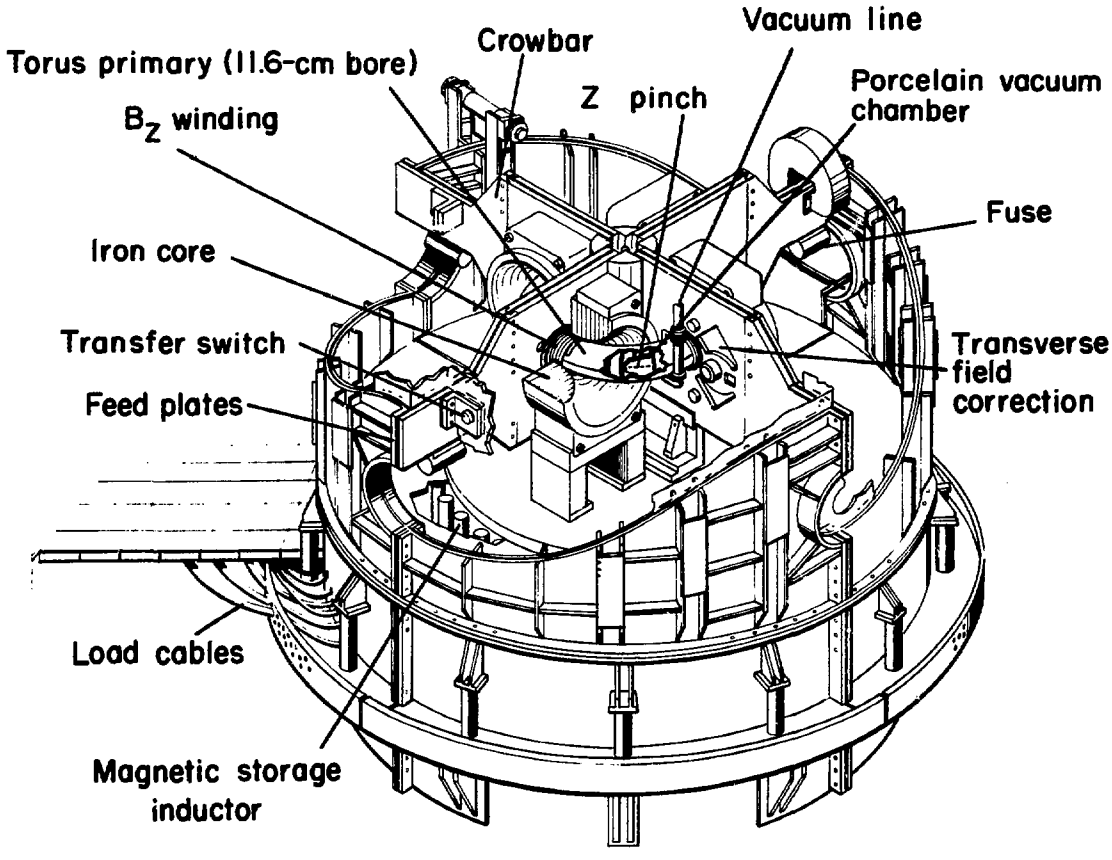

Fig. 1. Partially cut away drawing of the ZT-1 device.

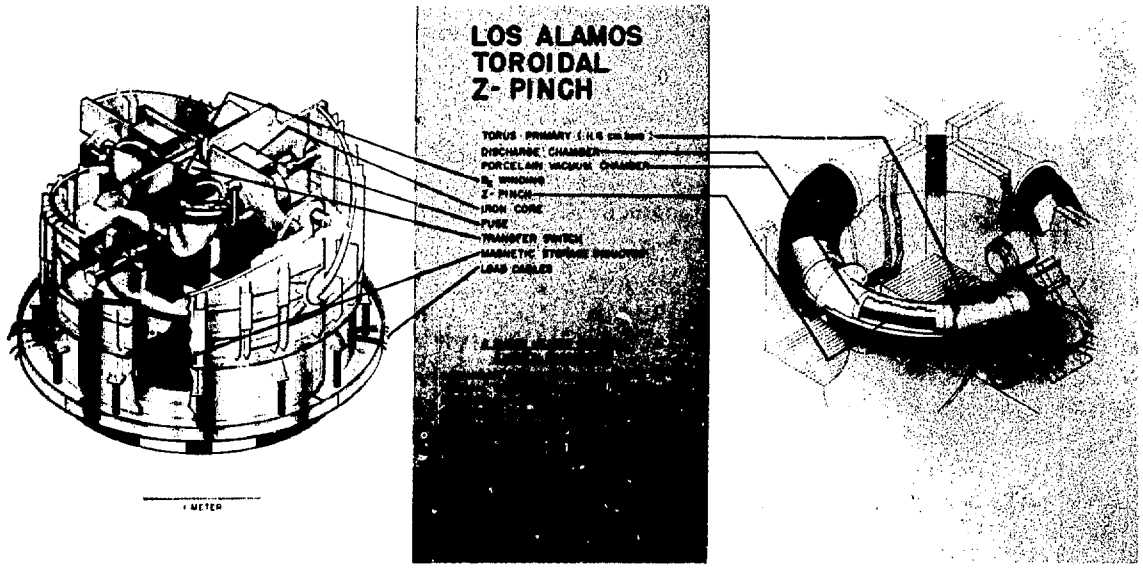

Fig. 2. Partially cut away drawings of the ZT-1 device.

32-turn coils per quadrant; again all drives are in parallel.

Since the primary is connected at four feedpoints to the parallel plate transmission lines, the four primary sections are electrically in parallel; the secondaries, or plasma discharge, are in series. The parallel plate lines at the feedpoints are 0.76 m wide with 1.2-mm insulation thickness to provide low inductance. Because the current flow along these lines is transverse to the torus, magnetic fields transverse to the discharge result unless the current flow pattern is controlled and forced to have the same azimuthal distribution, ideally, as the plasma image current inside the primary. This is accomplished by inductive cut out sections in the transmission lines as shown in Fig. 1. In addition, split copper cylinders are inserted inside the primary at each feedpoint to divert the residual transverse field. These field correction devices and the related test measurements are discussed in more detail in Sec. V. Also, analysis of field perturbations introduced by the pump port tubulations is given in Sec. V.

The vacuum chamber inside the primary is formed from ninety 10.3-cm-i.d., 4-mm wall thickness ceramic (99.8% purity vitrified Al_2O_3) sectors.

The ceramic pieces were ground and tapered to form 4° sectors for the torus. Overlapping step joints are provided at the edges of the sectors with a gap at the outer edges for insertion and seating of Viton O-rings. Under vacuum, the O-rings compress by $\sim$ 0.5 mm and form a reliable seal. This compression causes the inner lip of the ceramic step joint to close. The O-ring at the other end of the joint is shielded from the plasma discharge. Quartz window inserts provide viewing ports for diagnostics in two sectors. Two 1.2-cm-i.d. pump-out tubes are provided at the top and bottom of one sector in each quadrant of the assembly. These connect through flexible bellows to the vacuum manifold. Vacuum of 3×10^{-6} Torr is obtained with this system using a 260 ℓ/s turbomolecular vacuum pump in parallel with a 500 ℓ/s Vaclon pump.

Close spacing tolerances are maintained to minimize inductance. The total gap between the o.d. of the ceramic and the i.d. of the primary, including O-ring extension and insulation, is $\sim$ 2.5 mm.

A laminated magnetic core is inserted in each quadrant to improve the coupling efficiency of the primary circuit to the discharge. With the magnetic core, the magnetization current in the primary circuit is reduced by more than two orders of magnitude so that primary current has nearly the same value as the current in the plasma discharge. Also, with the reduced magnetization current flowing on the outside of the primary, the problem of field errors (see Sec. V) introduced by this current component becomes minimal and only the image current correction need be considered. The core design is discussed in Sec. VI.

III. MAGNETIC FIELD PROGRAMMING AND THE ELECTRICAL SYSTEM

A. Stable Field Configurations and Programmed Field Stabilization

MHD theory shows that there are stable diffuse z-pinch configurations capable of plasmas of high β_θ's($\sim$ 0.5). The specific stability conditions that must be met are described in the literature.[11-14] The magnetic field and plasma pressure distributions shown in Fig. 3 form a typical stable configuration. To reproduce such a theoretical configuration in the experiment, the field programming sequence illustrated in Fig. 4 is followed. The radial behavior of the fields during the discharge is shown at the top of the figure. The center two curves show the I_θ and I_z current wave forms. At the bottom of the figure, the magnetic field and plasma pressure profiles are shown at selected times in the discharge. The third

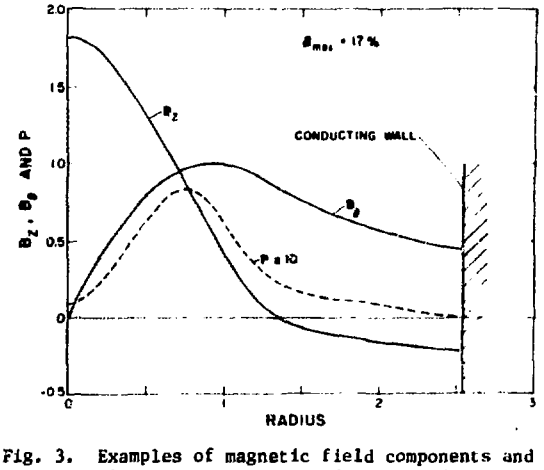

Fig. 3. Examples of magnetic field components and plasma pressure, as a function of radius for stable pinch configuration in ZT-1.

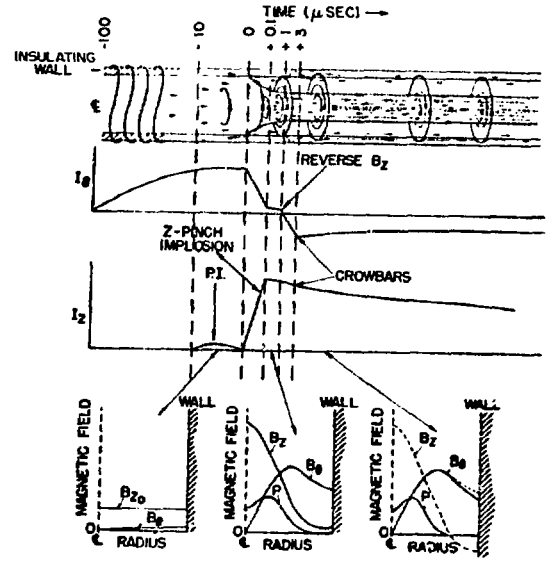

Fig. 4. Schematic summary of the magnetic field programming sequence required in ZT-1.

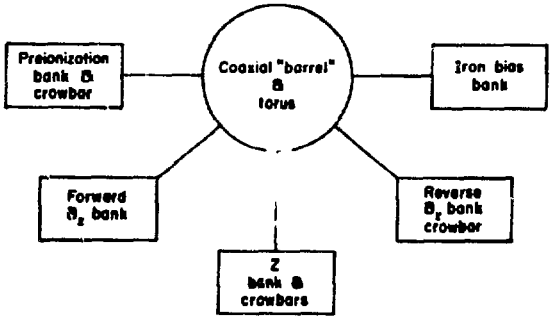

Fig. 5. Block diagram of the energy stores associated with the ZT-1 device, namely the preionization bank and its crowbar, which takes the plasma from a feeble rf glow to a plasma about 100% ionized; the iron bias bank, which returns the iron to a starting condition allowing the maximum volt-second flux change of the iron; the Z bank and its crowbars, which sets up the main flow of current in the plasma torus; the forward B_z bank, which sets up the bias magnetic field along the major axis of the torus; and the reverse B_z bank, which can be timed with respect to the Z bank.

profile should duplicate a theoretically stable configuration like that in Fig. 3, with the distributions controlled by the timing and magnitudes of the toroidal B_z field, reverse B_z field, plasma current, plasma pressure, and the crowbars which hold or limit the magnitudes at appropriate values.

At ∿ 100 μs before the main Z-pinch current is initiated, a B_z stabilizing field is turned on. About ∿ 20 μs before the main Z pinch, a ≲ 15-kA preionization Z current is passed through the filling gas. The main Z-pinch implosion then compresses the plasma and B_z bias field about the axis, heating the plasma. At selected times the I_θ in the external winding is made negative by reversing the voltage across the coil. This produces a reversed B_z field outside the pinch column. Finally, at ∿ 3 μs, the I_θ and I_z currents are crowbarred. The electrical system, shown in the block diagram in Fig. 5, comprises five capacitor banks and four crowbar devices used in initiating and rapid programming of the discharge.

B. B_z Circuit

The circuit for producing the toroidal stabilizing magnetic fields is shown in Fig. 6. This circuit is designed to provide the initial forward B_z field then reverse the field outside the plasma after the pinch is initiated. In the circuit diagram, the capacitor bank at the left, comprising C_1, C_2, and C_3, is set up as a three-stage Marx circuit with ignitron switching. This part of the circuit generates the initial bias or forward B_z. The effective bank capacitance is 160 μF with a maximum energy rating of ∿ 72 kJ and a maximum current of ∿ 20 kA into the load. At maximum current, 5 kA per

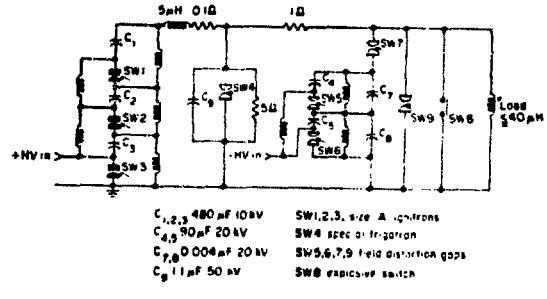

Fig. 6. Schematic electrical diagram of the B_z system used in ZT-1.

quadrant, a toroidal field of ∿ 6 kG is produced at the axis of the torus. The forward B_z current is more than critically damped and reaches peak in about 60 μs.

The B_z winding has two variations depending upon the specified magnitude and rate of change of the magnetic field. To obtain the maximum magnitude of forward and reverse B_z, a 66-turn coil of #8 wire is placed around each quadrant of the torus and all four coils are then electrically connected in parallel.

The rate of change of reverse B_z is increased by a factor of two with two 32-turn coils of #8 wire around each quadrant. All eight coils are then electrically connected in parallel.

Referring to Fig. 6, the 5-μH and 0.1-Ω circuit elements are cable inductance and resistance, respectively, and are inserted to limit the current supplied by the forward Marx when the crowbar, Sw4, is fired. C_1 and the 5-Ω resistor are provided to roll over the leading edge of the voltage waveform supplied from the forward Marx and prevent cable doubling which overstresses Sw4 and causes prefire problems.

The reverse B_z circuit is a two-stage Marx circuit with spark gap switches Sw5, Sw6, and Sw7. The effective bank capacitance is ∿ 45 μF with a maximum rated energy of 36 kJ and a maximum current of ∿ 25 kA into the B_z windings. The risetime of the reverse field is ∿ 30 μs and the maximum dB_z/dt ∿ 0.1 T/μs in a vacuum. The field distortion spark gap, Sw9, and the explosive switch, Sw8, serve as alternative methods of crowbarring the B_z system.

In the programmed firing sequence of the B_z system, the forward B_z system is fired, Sw1, Sw2, and Sw3 followed, at ∿ peak B_z field, by the first crowbar, Sw4. The pinch current I_z is fired ∿ 0.5 μs after Sw4 and the reverse B_z system is fired ∿ 1 μs before or after I_z. Finally the second crowbar, Sw8 or Sw9, is fired a few μs following the reverse B_z system.

C. Magnetic Core Back-Bias Circuit

The plasma current, I_z, is coupled to the primary current by nickel-iron magnetic cores; we use the terms "iron cores" and "iron" synonymously. The maximum core cross section that can be accommodated in each quadrant is ∿ 0.0425 m^2. The cores are designed to accept a $\dot{B}$ of 3×10^{10} G/s, or 300 V/cm^2, therefore requiring substantial insulation between both core laminations and groups of laminations. Because of the insulation requirements, a stacking factor of ∿ 0.70 is achieved (or equivalent to about 300 sq cm of iron) with a volt-second rating of ∿ 4.4×10^{-2}. To use the iron available most effectively, the cores can be back-biased to saturation in the negative direction thus using the volt-seconds from negative to positive saturation (∿ 8.8×10^{-2} Vs), a factor of two gain.

The circuit used for back biasing the iron is very simple, Fig. 7, consisting of a capacitor C_1, and four separate inductors L_1, L_2, L_3, and L_4, each in series with a loop around one core CR_1, CR_2, CR_3, CR_4. The inductance of a loop around a core is ∿ 80 μH, thus the series inductors determine the current value to first order. The circuit provides for drives of 0 to ∿ 900 A/m, which allows setting the reverse bias from 0 to well past saturation. The period of the bias circuit is ∿ 2.3×10^{-3} s. The large value of series inductance provides a very high impedance to the preionization and main Z currents which are coupled to the bias circuit by the cores. The large inductance also allows only ∿ 400 V max to be applied to the gas in the torus--not sufficient for ionization.

D. Preionization Circuit

The preionization circuit, Fig. 8, is composed of a "pre-preionization" circuit (C_2, Sw4, and R_2)

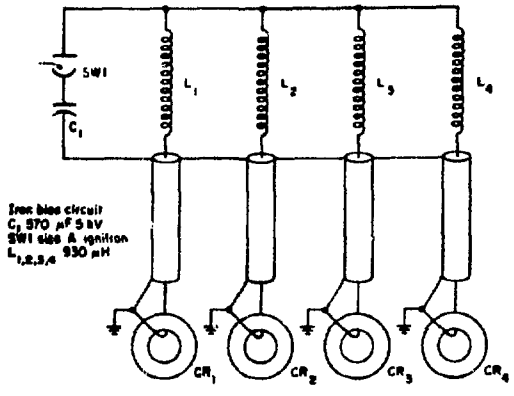

Fig. 7. Schematic electrical diagram of the iron biasing circuit in ZT-1.

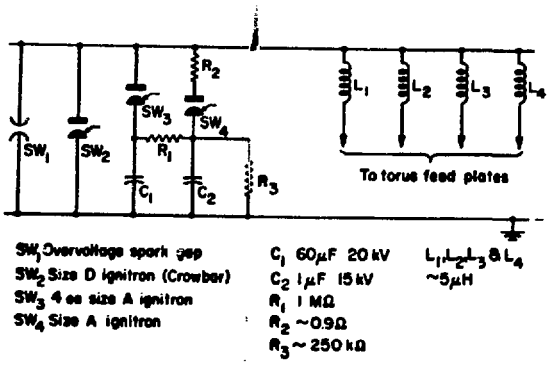

Fig. 8. Schematic electrical diagram of the preionization capacitor discharge circuit.

in series with the feed inductance's L_1, L_2, L_3, L_4, and the torus. This circuit, like the main preionization circuit, provides ∿ 5 kV max to each quadrant to initiate ionization. The circuit is heavily damped and has an RC decay of ∿ 1 μs. Its purpose is to initiate breakdown of the gas. Without this low-voltage bank the inherent delay in the gas breakdown of ∿ 1 μs would result in the total voltage of the preionization bank being developed at the torus. Under some conditions of operation this high voltage would cause the switches in the main I_z bank to fire.

The main preionization bank C_1, and Sw3, charged up to ∿ 15 kV, supplies sufficient energy to ionize the gas completely. The voltage divides between the torus inductance and the feed inductances, L_1, L_2, L_3, and L_4. The maximum current is ∿ 20 kA per quadrant, with a period of ∿ 55 μs.

The inductances L_1, L_2, L_3, and L_4 include the coaxial cable from the preionization bank to the machine and the feed system inductance at the machine. This rather large inductance prevents excessive current from flowing into the preionization system from the Z bank when it is fired. Sw1 is a simple overvoltage gap set to break down at ∿ 20 kV to protect the preionization components if the Z bank prefires. Sw2 allows the system to be crowbarred from the start of preionization current up to about peak current.

As a general aid in breaking down the gas, an rf generator at ∿ 29 MHz is coupled into one quadrant at the pump-out ports by an electrode inside a vacuum pump-out port.

E. I_z Circuit

The I_z circuit provides the primary current to the aluminum torus. The iron cores, Sec. VI, provide essentially unity coupling between primary and secondary. The difference current during the very fast risetime of the plasma current in the fuse mode is only ∿ 1.5% of the primary current.

The I_z capacitor bank is a two-stage inverting Marx circuit of ∿ 480-kJ maximum energy storage at 20-kV charge. The Marx circuit output, Fig. 9, is a dc ground through L_3 and L_2 as are the other Marx circuits in the system, thus ensuring that the machine is safe to work on at all times, except during the firing cycle.

In operation, in the fuse mode, C_1 and C_2 are charged to some voltage V_o. When Sw1 and Sw2 are fired, $-2\ V_o$ is applied to the cables feeding the machine. Current flows through L_4, made up of switch, capacitor, and cable inductance, and L_5, the drum inductance, and the fuse. The maximum current that can be supplied into a short circuit at the fuse is ∿ 1.5 MA per quadrant.

The plasma current can be crowbarred by Sw5 to limit the current to the range of 40 to 200 kA with $\dot{I}$ values of 2×10^{12} A/s.

Another variation of this circuit used in the experiment is to put a current limiting series

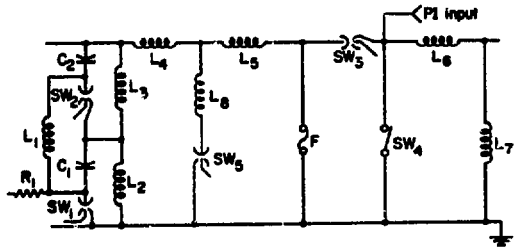

Fig. 9. Electrical schematic for ZT-1 inductive energy storage system.

resistor (R) in place of Sw3. The current risetime is now the L/R time constant of the circuit, which can be ∿ 0.6 μs, and decay time is RC, which is 75 μs.

Section IV gives a detailed discussion of the inductive storage and fuse system.

In the slow mode the fuse is removed and switch Sw3 is short circuited. When Sw1 and Sw2 are fired, C_1 and C_2 are discharged in series through L_4, L_5, L_6, and L_7. Primary current of up to 1 MA per quadrant can be supplied in this mode.

Sw4 is an explosive switch used to provide a metal-to-metal crowbar circuit (see Sec. V).

IV. DESIGN OF THE INDUCTIVE ENERGY STORAGE SYSTEM USING EQUIVALENT CIRCUIT COMPUTER CALCULATIONS

The electrical circuit schematic (Fig. 9) and the physical layout of the discharge circuit are described in Secs. II and III. The characteristics of the magnetic energy storage system with fuse switching have been previously reported.[15] This section presents the results of numerical calculations used to predict the operation of the experiment with fuses. Figure 10 presents a simplified schematic useful in understanding a multiple fuse system. The extrapolation from the one- to the four-fuse operation introduces the simultaneity question. Fuse tests show there is an average jitter of 0.2 μs with 0.5 μs being the maximum deviation. Inasmuch as the half-width of the voltage pulse also is ∿ 0.5 μs, such a large jitter would result in reduced electric fields and large nonbalanced currents in the drum. Hence there must be sufficient mutual coupling among the fuses to force simultaneous operation.

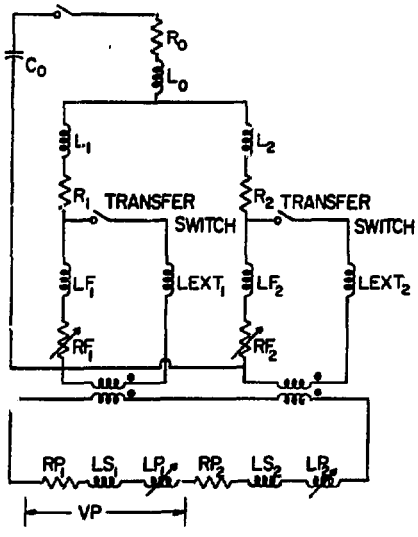

Fig. 10. Simplified schematic of multiple-fuse inductive energy storage circuit.

The equivalent circuit shown in Fig. 10 is used to analyze a two-fuse coupled circuit rather than the four-fuse system actually used. Energy storage occurs in L_0, while coupling between fuses is limited by L_1, L_2 and R_1, R_2. The fuses appear as variable resistors RF_1 and RF_2. At a predetermined voltage, the transfer switch is closed and current is transferred to the Z pinch. Coupling is accomplished by a transformer which is assumed to be ideal. The Z pinch appears as variable inductances LP_1 and LP_2, whose functional dependences are derived from the snowplow model. An initial B_z bias field is included in the calculation, subject to the flux conservation conditions. Plasma pressure is not included; circuit parameters are calculated from the dimensions and geometry of the experiment. Experimental values of L_1, L_2, and LEXT1, plus LEXT2, are obtained using analogue measurements.

Figure 11 shows the current flow and magnetic field lines determined from a resistive analog for the case of mismatch in the operation of adjacent fuses. Current is diverted from one fuse to the other along the flow lines shown. From such results, the inductance between the fuses is calculated to be 14 nH.

Dynamic resistance of the fuses is determined from published tables,[15] which give values of resistivity as a function of internal energy up to the onset of fuse vaporization; beyond this, resistivity is determined from actual measurements.[16] The results are shown in Fig. 12 as plots of fuse resistivity versus internal energy density for copper foil. A least squares fit over three sections of the resistivity curve is used to give analytic expressions for use in the calculations.

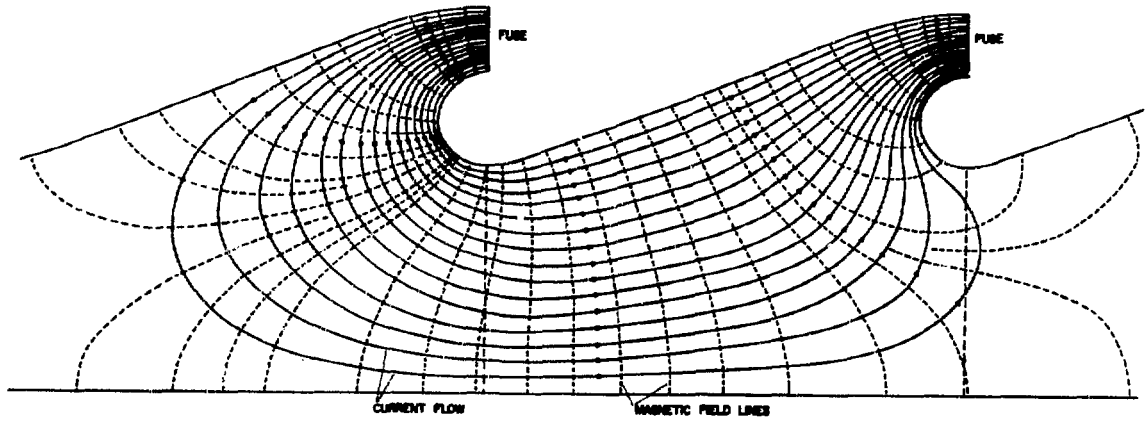

Fig. 11. Current flow and magnetic field lines for a case of mismatched fuses.

Resistivity (ohm-m)	Internal Energy Range (E in MJ/kG)
$\rho = 2.06 \times 10^{-8} \exp (4.51 \times 10^{-6} E)$	$0 \rightarrow 0.3$
$\rho = 4.98 \times 10^{-8} \exp (1.61 \times 10^{-6} E)$	$0.3 \rightarrow 1.3$
$\rho = 1.7 \times 10^{-7} \exp (0.665 \times 10^{-6} E)$	$1.3 \rightarrow 6.0$

To test the applicability of this equivalent circuit calculation, results of computed and measured waveforms for current and voltage for the single fuse case of the earlier linear Z-pinch experiment[5] are compared and agree within the experimental accuracy of $\sim$ 10% as shown in Fig. 13. (In this calculation, L_2 and R_2 are made very large so as to remove the second fuse from the circuit.)

For the toroidal case, the achievement of similar fuse-voltage characteristics is of primary importance. This is tested using the equivalent circuit calculations by introducing a timing difference of approximately three times the normal jitter between fuses by using different fuse cross sections ($S_1 = 35.0 \times 10^{-6}$ m^2 and $S_2 = 28.6 \times 10^{-7}$ m^2) in the two legs of the equivalent circuit. Results calculated using these cross sections with the single-fuse technique above show that the current and voltage waveform attain peak values with $\sim$ 2-μs time difference (Fig. 14). To determine the effectiveness of coupling of the fuses with this timing difference, the equivalent circuit calculations are repeated using the two different fuses with appropriate values of L_1, L_2 and R_1, R_2. Calculations show that the voltage characteristics coincide within 1% as in Fig. 15. The two voltage characteristics cannot be resolved from one another

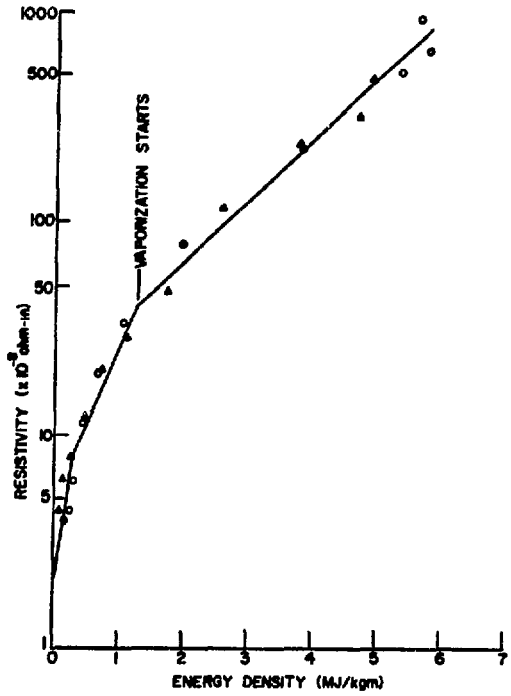

Fig. 12. Fuse resistivity as function of internal energy density for copper foil.

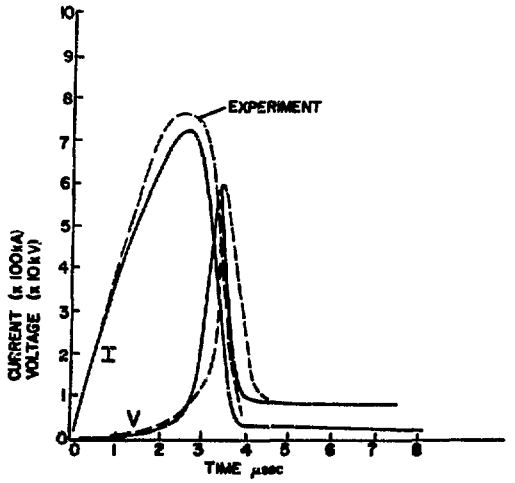

Fig. 13. Comparison of computed and measured current and voltage waveforms for a single fuse.

within the accuracy of this plot. Numerous firings of the four-fuse system confirm both simultaneity and reproducibility of the voltage waveform applied to the plasma.

Physically, the fuses are sheets of plastic, 0.25 m square, 0.02 m thick; along one edge the foil

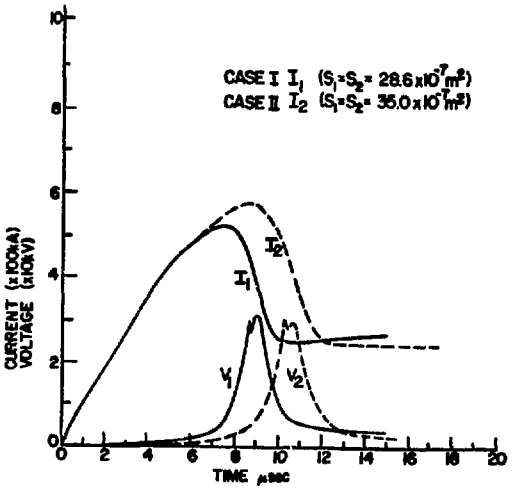

Fig. 14. Current and voltage waveforms resulting from foils of different thicknesses of copper.

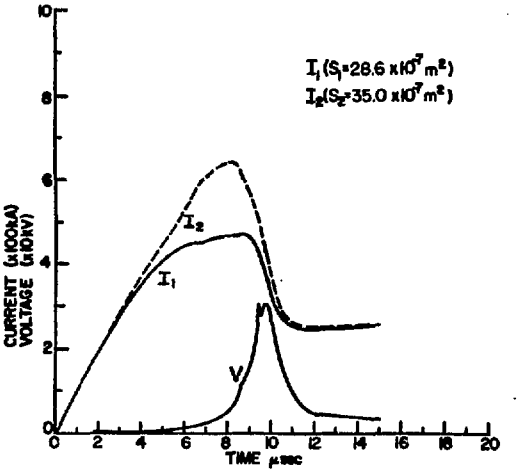

Fig. 15. Output voltage of mutually coupled dissimilar fuses cannot be resolved as the sum of two voltages.

is centered and also wrapped around that edge. A typical foil is copper, 2×10^{-5} m thick, 0.12 m wide, and 0.15 m long. Connections are made to the ends of the foil, away from this folded edge, and the entire foil section is immersed in a sealed pouch of glass beads 10^{-4}-m diameter. (See Fig. 16.) Details of construction may be found in the annual report[17] and design considerations in the

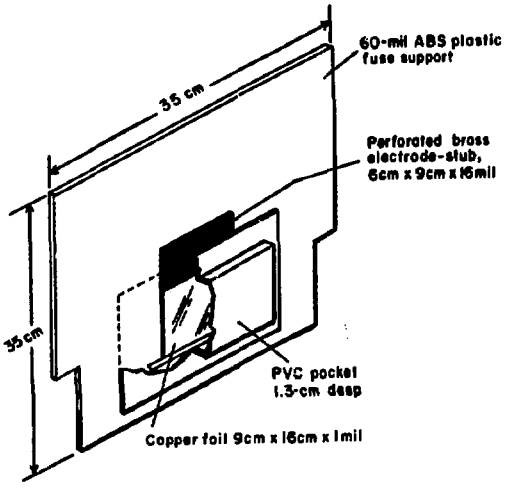

Fig. 16. Photograph of the fuse.

literature.[16,18,19] The fuse package readily absorbs 21 kJ of energy without destroying itself, and being a sealed unit, may be used in any position. This inverting feature can double the energy-handling capability of this fuse-driven system.

V. MAGNETIC FIELD ERRORS

In the theory of stable magnetic field configurations for the toroidal pinch, the fields are assumed to have complete toroidal axial symmetry and to be free from perturbations and nonuniformities. Even small magnetic field errors may have undesirable effects on plasma equilibrium and containment. This has been observed in Tokamak devices,[20,21] the Stellarator,[22] GGA Octupole,[23] and the G.A. programmed pinch device.[24]

In the ZT-1 device, the current through the parallel plate transmission lines at the torus feedpoints will produce a significant transverse field error within the torus in the region of the feedpoint gap unless corrections to the direction of current flow are made. The current through the lines can be considered as having two components--the magnetization current and the plasma image current. The magnetization current flows on the outer surface of the primary and provides the flux change that generates the toroidal electric field in the discharge tube. The use of iron cores reduces this current component to a sufficiently low value so that the field errors due to this source are very small. The plasma image current flows on the inner surface of the torus primary with an azimuthal distribution determined by the position of the plasma column inside the discharge tube. At the feedpoint gaps, this current must flow out and return along the parallel plate lines without producing magnetic field distortions in the region of the plasma. These distortions will occur unless special precautions are taken to obtain a radial current flow pattern in the transition region between primary and parallel plate lines.

A. Calculation of Equilibrium Plasma Image Current Distribution

The plasma image current density is proportional to the poloidal field at the inner surface of the primary. An axisymmetric toroidal MHD equilibrium computer code was used to compute the variation in this surface field for toroidal diffuse pinch equilibria having hollow pressure profiles and reverse toroidal fields outside the pinched plasma. Sample field and pressure plots for poloidal beta (β_p = average plasma pressure/magnetic pressure due to the average poloidal field at the wall) of 0.1, 0.4, and 1.0 are shown in Figs. 17a, b, and c, respectively. In the figures, the plasma pressure was varied to change β_p; all other parameters, including the shape of the plasma profile (as a function of poloidal flux), were held constant. In these examples the ratio of the peak plasma pressure to the pressure at the magnetic axis was 1.3. The peak of the poloidal field is held constant in this set of figures, so the primary change readily apparent in the poloidal field is the outward radial shift in the profile. The 6% change in the toroidal field is the adjustment it makes to maintain pressure balance.

A series of computer runs was made to see how the plasma profile width (at half-maximum) and β_p affect the poloidal field at the outer wall. Figure 18 shows the effect varying β_p has on the poloidal field at the wall for a fixed profile width. One notable feature of these calculations is that, for a given width of pressure profile, there is a β_p value at which the poloidal field magnitude along the conducting wall is nearly constant.

The value of the ratio of the maximum to minimum poloidal field along the outer wall of the torus

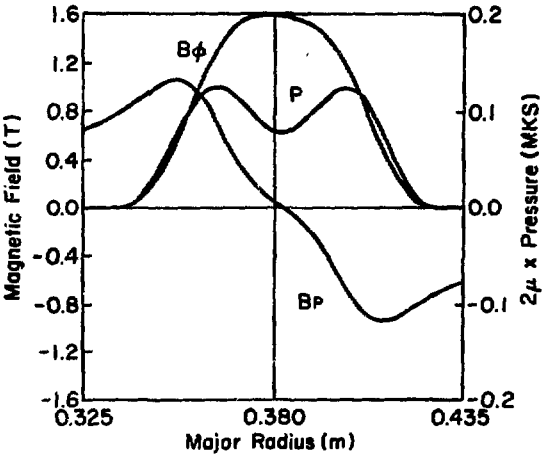

Fig. 17(a). Field and pressure plots for ZT-1 for a poloidal β value of 0.1.

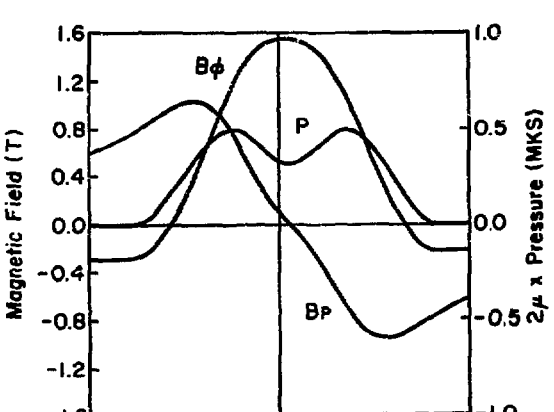

Fig. 17(b). Field and pressure plots for ZT-1 for a poloidal β value of 0.4.

cross section was used to aid in the feed plate design. Figure 19 shows both how the ratio of B_p at R_{max} to B_p at R_{min} varies with β_p and width of the plasma profile. In each case, the general shape of the pressure profile remains the same. For example, the ratio of plasma peak to plasma value at the magnetic axis remained constant, and all the parameters that determine profile shape were scaled by the width parameter. The variation of field ratio with β_p is virtually linear for a given plasma profile

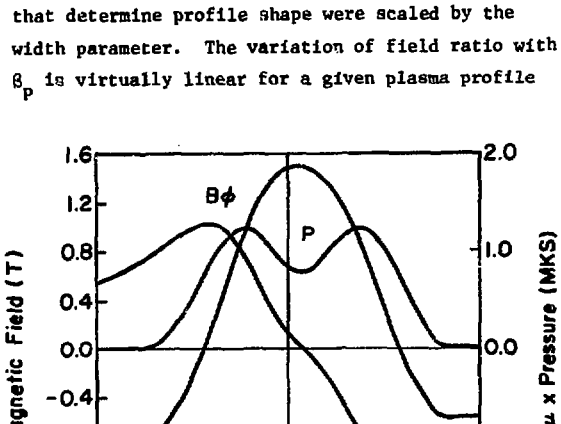

Fig. 17(c). Field and pressure plots for ZT-1 for a poloidal β value of 1.0.

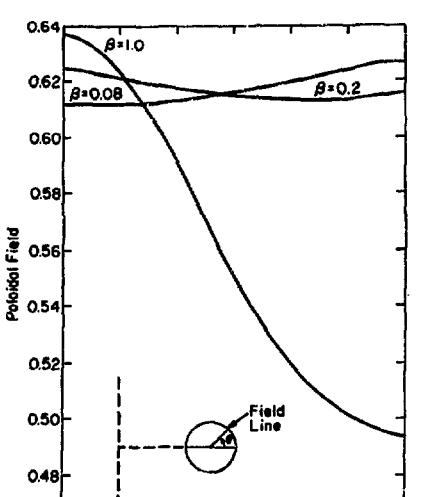

Fig. 18. Poloidal field variation along a field line near conducting boundary for a ratio of plasma width at half-maximum to conducting boundary diameter of 0.55.

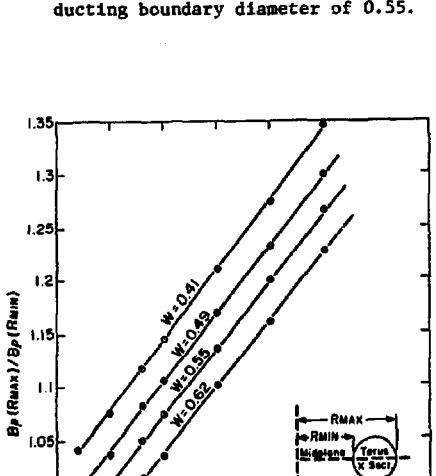

Fig. 19. Poloidal field ratio at conducting wall of ZT-1 as a function of plasma profile and poloidal β.

width. MHD stability calculations indicate that the plasma width should be greater than about one-half the conducting boundary diameter and that β_p should be less than 58%. Desirable operating conditions are well below these critical stability limits, thus a design which allows poloidal field variations up to 10% along the minor circumference is adequate.

The variation of the magnetic center shift with β_p and width is shown in Fig. 20. The greatest shift occurs at high beta and with narrow plasma profiles. The variation of shift with β_p is approximately linear for a given width.

B. Measurement and Correction of the Feedpoint Magnetic Field Error

Two full-scale mock-ups of the feedpoint section were used to determine the transverse field error and to test the effectiveness of corrective measures.

The first mock-up consisted of a parallel plate transmission line of the same width and length as those in ZT-1, and two aluminum straight cylindrical tubes of 11-cm i.d. to simulate the torus primary. Since the above theoretical calculations indicate a nearly uniform poloidal distribution of toroidal current for plasma equilibrium, the effects of toroidal curvature were neglected. The outer ends of the cylindrical sections were closed off by metal plates joined by an axial 1.6-cm-diameter rod that simulated the plasma current. The mock-up circuit was driven by a damped oscillatory discharge (∿ 5 kA, 15-μs period) connected to the parallel plates at the position of the transfer switch in ZT-1.

Measurement of the initial field asymmetry before modifications was made with a single-turn flux loop mounted on an ∿ 11-cm-diam cylindrical phenolic form inside the simulated primary. The loop was rotated to measure the magnitude and azimuthal variation of the poloidal field at the feedpoint. The results, shown in Fig. 21, indicate a transverse field superimposed on a constant poloidal B_θ component. The magnitude of the field due to the ∿ 5 kA axial current at the position of the flux loop was 198 G -- indicated by the dashed line in the figure. Superimposed on this is a transverse field error at ∿ 45° (≈ 20% of B_θ) that adds to the B_θ component at $\Theta = 0^\circ$ at the side of the feedpoint nearest the current input, and subtracts at 180° on the opposite side of the primary. (This field error is of approximately the same relative magnitude reported by Kerst et al.[24])

Three techniques for eliminating this field error were tested: (a) a split ring cylindrical flux divertor inserted inside the simulated primary across the feedpoint gap, (b) grooved interlocking flanges in the parallel plate lines coaxial with the primary, and (c) current distribution control by cutting inductive gaps in one of the parallel plates.

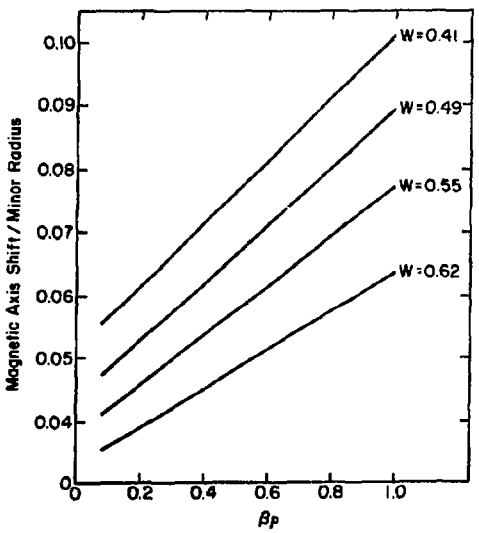

Fig. 20. Magnetic axis shift as a function of plasma profile width and poloidal β.

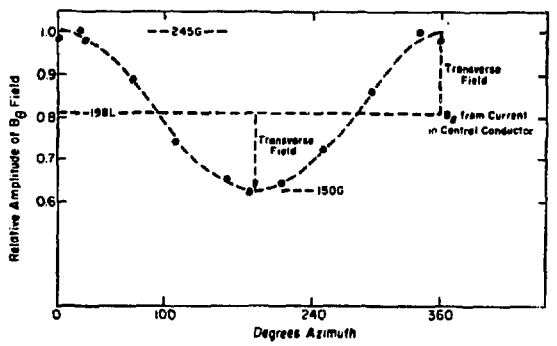

Fig. 21. Variation of poloidal magnetic field component around minor circumference due to transverse field error. Measurements made with full-scale mock-up.

Measurements of the magnetic field were made with flux loops oriented to measure transverse, axial, and poloidal field components. Results of measurements of the reduction of the transverse field error with cylindrical divertors of 4-, 7-, and 15-cm length are shown in Fig. 22. Copper cylinders of 0.08 cm thickness were used with 0.25-cm-thick insulation to avoid short circuiting the feedpoint gap. Also, an insulated longitudinal gap was cut in each cylinder, necessary in the ZT-1 system to admit the toroidal stabilizing field. These cylindrical inserts tend to shield the volume inside the feedpoints and divert the transverse field away from the discharge region. However, the shielding is limited because there remain flux paths around the ends of the divertors, and the reluctance of the magnetic path is changed significantly only by the longer cylinders. The extension of the transverse field flux lines around the ends of the divertor cylinders was apparent in measurements with flux loops mounted on a coaxial Lucite cylinder that was moved along the axial conductor. The effectiveness of the shielding increased with divertor length but there was also a corresponding increase in the system inductance because of the insulation space required. Because of this factor, the divertors used ultimately in the ZT-1 machine were limited to $\sim$ 6-cm long, 11° sectors. From Fig. 23, these should decrease the transverse error field by only a factor of $\sim$ 2 and additional field corrective measures are needed.

This mock-up was also used to test the effectiveness of reducing the error field by means of circular tongue and groove patterns[25] machined into the parallel plate lines concentric with the primary. Two such tongue and groove sections were machined into the mock-up header at 21- and 22-cm radii with oppositely directed groove depths of 1.25 cm and 1.75 cm. The reduction of the transverse field inside the primary at the feedpoint gap was a factor of $\sim$ 2. Deeper tongue and groove sections at smaller radii--nearer the primary--should be more effective. But because of the difficulties involved in insulating these areas for $\sim$ 80 kV, this technique was not used in ZT-1.

The technique of machining slots in one of the parallel plate transmission lines to control the current distribution was adopted for the ZT-1 system. The slotted areas are effectively trimmed inductances which are varied by changing the length

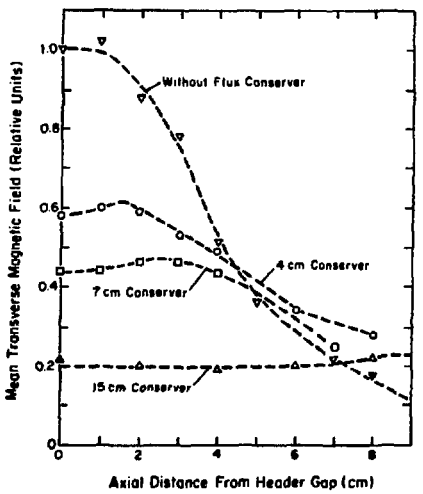

Fig. 22. Measurements of reduction in transverse magnetic error field with metal cyclinders or flux divertors of indicated lengths inserted across the feedpoint gap of the mock-up.

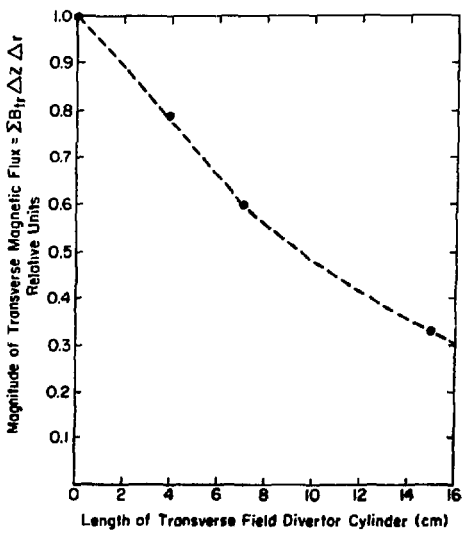

Fig. 23. Magnitude of transverse magnetic field error versus length of flux divertor cylinder inserted at the feedpoint gap of mock-up.

and width of the holes. A first approximation to the distribution and size of the slots required was obtained using the resistor paper analog method. The paper was cut to scale to simulate one of the parallel plate lines and the current flow pattern traced with probes. Holes were cut in the resistor paper to force the current distribution, at the position of the primary to transmission line junction, to have only a radial component toward the primary axis, and to have a uniform current density around the primary circumference.

A second full-scale mock-up of one of the parallel plate lines was then constructed with the slot pattern determined from the resistor paper analog tests. The mock-up circuit was driven by a capacitor discharge connected at the position of the transfer switch. A feedthrough bolt at the position of the torus axis was used to complete the circuit. A thin phenolic disk containing magnetic field probe coils was mounted between the plates and rotated about the feedthrough bolt. The probe coils were oriented to measure the azimuthal and radial field components at the radius of the primary inner surface. Further modifications of the slot pattern were made by trial and error until a uniform azimuthal field distribution with $\gtrsim$ 2% variation was obtained. The final transmission line layout is shown in Fig. 24. The plates are held together by three insulated through-bolt clamps inserted through the counterbored holes shown in the figure. The additional three areas cut out of the plate to control the current distribution are labeled A, A', and B. Trimmer bars are inserted across A and A', as shown, for additional control of the current flow. Without the cutouts A, A', and B, the asymmetrical field distribution shown in Fig. 25(a) is obtained. With the holes, A, A', and B cut out, the field variation shown in Fig. 25(c) is obtained. The field error is overcompensated so that the field asymmetry is then reversed with the higher current density, j_r, on the side of the primary opposite the transfer switch position. This pattern would be used if the plasma equilibrium is off center by 4 mm as described above—see Figs. 19 and 20. With the insertion of 7-mm-wide trimmer bars at 2.5 cm from the ends of gaps A and A', the uniform current distribution shown in Fig. 25(b) was obtained. This "uniform current" configuration was assumed in the ZT-1 experiment.

C. Field Errors in Poloidal and Toroidal Field Due to Pump Port Perturbations

There are two 1.9-cm-diameter pump ports in each quadrant of the aluminum primary of the ZT-1 device. The holes allow the use of 1-cm-i.d. ceramic tubes for evacuation of the discharge tube. The magnetic field perturbations on the poloidal and toroidal field components caused by these holes have been examined numerically.

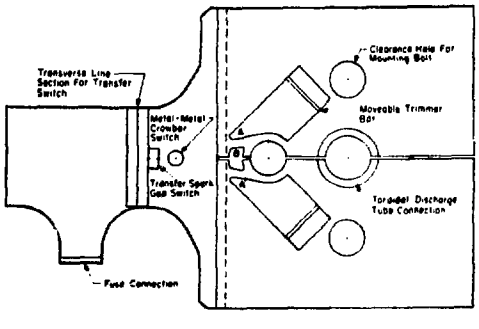

Fig. 24. Final pattern of the parallel plate transmission line section extending from the fuse to the torus feedpoint showing the mounting holes for through-bolt clamps and the pattern of inductive cutouts to control current flow and minimize transverse magnetic field error.

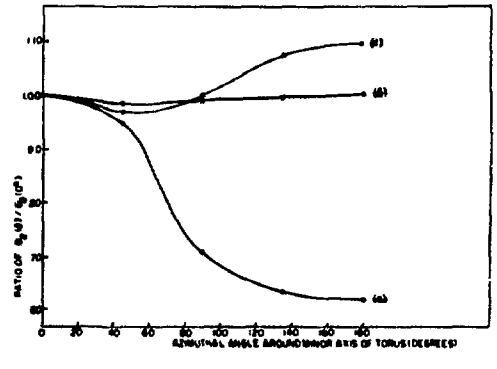

Fig. 25. Azimuthal feed plate field distribution; undercompensated (a), overcompensated (c), and correctly compensated with trimmer bars (b).

1. Toroidal Field Perturbations. Since calculation of field divergence into round holes in the primary is difficult, the model used for computation assumed a cylinder the dimensions of the primary with an azimuthally symmetric cut, 1.9 cm wide, taken around the minor circumference. A 2.85-cm-diam coaxial center conductor was assumed to simulate the plasma pinch. This forced the B_z field lines at this radial position to be parallel to the minor axis. A numerical axially symmetric equilibrium code then determined the position of B_z field lines and the strength of the magnetic field. In Fig. 26 the strength of the B_z field is plotted along a radius in the plane midway in the cut, showing a comparison of calculated and experimental results obtained with probes. The field drops off as expected with a 21% reduction at the pump port, r = 5.2 cm. Flux lines $\sim$ 2.5 mm from the porcelain wall will intersect the wall at the cut. As a round hole would have a smaller effect than the cut assumed in the calculation, a displacement of $\lesssim$ 2 mm is possible.

2. Poloidal Field Perturbations. The geometry shown in Fig. 27 was used to compute the distortion of the poloidal field by the pump ports. The

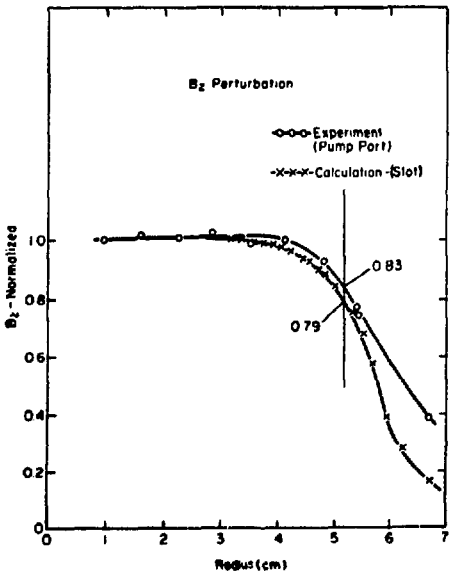

Fig. 26. Results of computed and measured values of magnitude of the B_z field along a radius through a pump port.

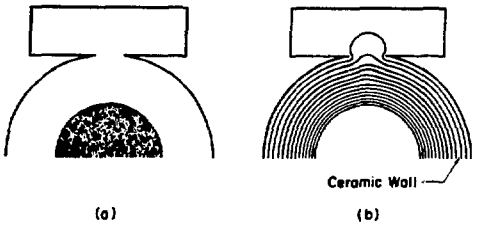

Fig. 27. The radial displacement of poloidal lines at the region of a pump port.

dimensions are those of ZT-1 with an inside conductor that carried a Z current either one-half or three-quarters the diameter of the primary. The model assumed for computation assumes two slots (one not shown) that are continuous around the major circumference and located on the median plane at the position of the pump ports. Figure 27a shows the conductors and Fig. 27b shows the computed poloidal flux lines. The maximum deflection of the field lines at the slot (or pump port) is about 2 mm at the ceramic wall.

VI. MAGNETIC CORE DESIGN

The use of magnetic cores with toroidal discharges offers three advantages: (1) reduced expansive hoop forces on the primary, (2) reduced field errors at the feedpoints caused by the magnetization current which is decressed by > 2 orders of magnitude with the use of the cores, and (3) more efficient use of the current since the magnetization component is decreased.

Four magnetic cores are used in the experiment. Each core is made up of seventeen 0.44-m-wide tape-wound sections. The sections have an outer diameter of 0.686 m and inner diameters varying from 0.25 to 0.594 m to accommodate the curvature of the toroidal discharge tube. The ferromagnetic tape is made of 50/50 nickel-iron alloy of 0.0254-mm thickness and 12.7-mm width. The stacking factor is $\sim$ 0.8 and the material resistivity is 45×10^{-8} Ω-m.

The thin tape is chosen to permit rapid penetration of the magnetic flux into the core with minimal applied magnetization current. A typical voltage waveform required for the experiment is shown in Fig. 28. The magnetization current required to induce this voltage is calculated using the saturation wave theory of Wolman and Kaden.[26] This approach was used by Winter, Kuenning, and Berg[27] to determine the magnetization current necessary to

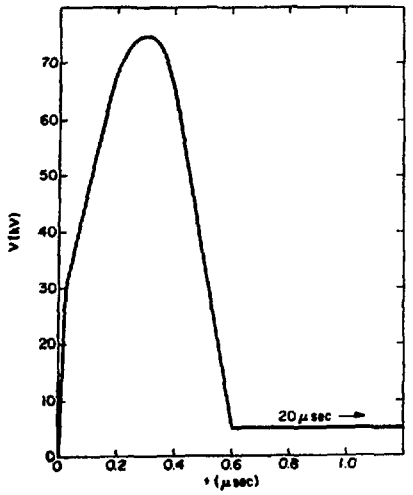

Fig. 28. Assumed voltage V per quadrant as function of time, t.

produce given voltage pulses in single magnetic sections for the Astron device.

To calculate the performance of a combination of sections having different inner diameters, it is convenient to calculate first the voltage induced in a single section by a given magnetization current I(t). The voltage $V_n(t)$ induced in a section of index n is (in MKS units):

$$V_n(t) = 2\,\frac{Sw}{d}\sqrt{\frac{\rho\,\Delta B_s}{\pi}}\;\frac{I(t)}{\sqrt{\int_0^t I(t)\,dt}}\left(\sqrt{r_{on}}-\sqrt{r_{in}}\right),$$

where w, d, ρ are the width, thickness, and resistivity of the tape material, S is the stacking factor, and ΔB_s is the magnetic field change at the saturation wave front. The value for r_{in} is given by

$$r_{in} = r_{in} \text{ for } r_s < r_{in} \quad ,$$

$$r_{in} = r_s \text{ for } r_{in} \le r_s \le r_{on} \quad ,$$

$$r_{in} = r_{on} \text{ for } r_s > r_{on} \quad ,$$

where r_s is the radius of saturation given by

$$r_s = \frac{4\rho}{\pi d^2 \Delta B_s}\int_0^t I(t)\,dt \quad ,$$

and r_{in} and r_{on} are the inner and outer radii of the n-th section. The equations for $V_n(t)$ are summed over all sections making up a core to give the total induced voltage V(t). The term I(t) is factored out and the expression solved numerically to give the magnetization current I(t) for a given voltage V(t). Figure 29 shows the magnetization current as a function of time corresponding to the voltage trace of Fig. 28 for two values of ΔB_s determined by the magnitude of the magnetic field reversal. The cores become saturated at 9 or 11 μs for the values of ΔB_s chosen. Before saturation, the magnetization current remains orders of magnitude below the ∿ 200-kA plasma current.

From the magnetization current, the interlaminar voltage is readily calculated. The highest value occurring in the core is shown in Fig. 30 as a function of time for the two values of ΔB_s. During the initial peak, the highest voltage occurs at the inner diameter of the core with a peak value of 1 V which is below the 2-V limit set by the manufacturer. Near saturation, the highest interlaminar voltage occurs at the periphery. The large theoretical increase in voltage at full saturation coincides with the steep increase in the magnetization current and is damped by the finite impedance of the

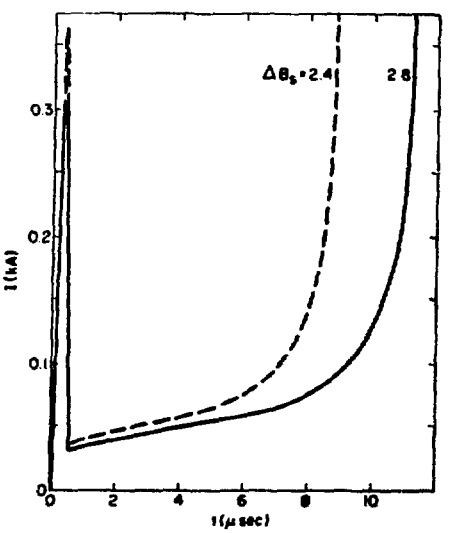

Fig. 29. Calculated magnetization current I as function of time t for two values of magnetic field reversal ΔB_s.

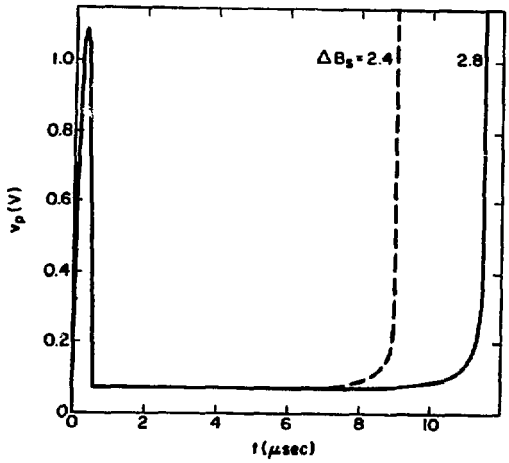

Fig. 30. Highest interlaminar voltage v_p in the magnetic core as function of time, t, for two values of magnetic field reversal ΔB_s.

energy storage circuit. In operation, no arcing of the cores has been observed.

VII. METAL-TO-METAL CROWBAR SWITCHES

Low-inductance crowbar switches have been installed in the four feedplates of ZT-1. The design of this switch is shown in Fig. 31 and detailed by Dike and Kewish.[28] Characteristics of the switch include a self-inductance of ∿ 3 nH, and a resistance of ∿ 5 μΩ. Time of closure and jitter is ∿ 11.0 ± 0.3 μs (where t_o = 0 is defined as the start of current in the bridgewire of the detonator). Crowbarred currents ranging between 180 and 330 kA show, without burning of the current contact, L/R decay times of 1.2 ms. Performance on the ZT-1 experiment is within these electrical parameters, although complicated by the plasma load.

ACKNOWLEDGMENTS

The authors wish to express their gratitude to J. L. Tuck, R. F. Taschek, H. T. Motz, and F. L. Ribe for discussions and encouragement, and to E. L. Kemp, R. Kewish, and R. Haarman for engineering support. Thanks for technical assistance in the assembly, maintenance, and operation of the experiment are given with pleasure to A. Brousseau, W. Bowman, D. Burkett, C. Charlton, R. Holm, L. Iko, D. Jardine, A. Lopez, A. Rendon, and N. Salazar.

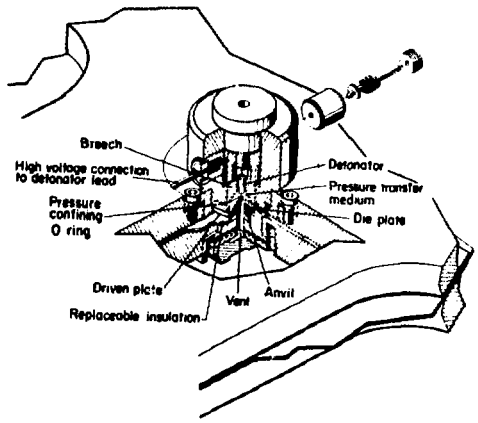

Fig. 31. Partially cut away drawing of explosive crowbar switch for ZT-1.

REFERENCES

1. T. Ohkawa, H. K. Forsen, A. A. Schupp, Jr., and D. W. Kerst, "Toroidal Discharge Experiments with Rapid Programming," Phys. Fluids 6, (1963) p. 846.

2. D. C. Robinson and R. D. King, "Factors Influencing the Period of Improved Zeta Stability," Proceedings, Plasma Physics and Controlled Nuclear Fusion Research, Novosibirsk, 1, (August 1968), p. 263.

3. C. Bobeldijk, R. J. J. Van Heijningen, P. C. T. Van Der Laan, L. Th. M. Ornstein, W. Schuurman, and R. F. De Vries, "Properties of a Toroidal Screw Pinch Surrounded by a Constant-Pitch Magnetic Field," Ibid, p. 287.

4. R. Wilhelm and H. Zwicker, "Experimental Observations on a Toroidal Screw Pinch," Zeitschrift Fur Physik 240, (1970), p. 295.

5. J. N. Di Marco and L. C. Burkhardt, "Z Pinch Driven by Magnetic Energy Storage," Proc. IV European Conf. on Controlled Fusion and Plasma Physics, Rome (August 1970), p. 53.

6. J. A. Phillips, "Proposal for A Shock-Heated Toroidal Z-Pinch Experiment," Los Alamos Scientific Laboratory report LA-4352, November 1969.

7. M. N. Rosenbluth, "Infinite Conductivity Theory of the Pinch," Los Alamos Scientific Laboratory report LA-1850, (September 1954).

8. J. N. Di Marco and L. C. Burkhardt, Los Alamos Scientific Laboratory Controlled Thermonuclear Research Program Annual report, LA-4351-MS (1969), p. 54.

9. M. V. Clauser and E. S. Weibel, Proc. Second U. N. Conf. on Peaceful Uses of Atomic Energy, 32, (1958), p. 161.

or L. O. Heflinger and S. L. Leonard, Div. of Plasma Phys., APS, Monterey Conf., J3 (1959).

10. H. A. B. Bodin, A. A. Newton, and N. J. Peacock, Nuclear Fusion 1, (1960), p. 54.

11. D. C. Robinson, Plasma Phys. 13, (1971), p.439.

12. D. A. Baker, L. C. Burkhardt, J. N. Di Marco, P. R. Forman, A. Haberstich, H. J. Karr, L. W. Mann, J. A. Phillips and A. E. Schofield, Plasma Physics and Controlled Nuclear Fusion Research, Vol. I, Madison, Wisconsin (1971), p. 203.

13. A. Haberstich, Los Alamos Scientific Laboratory Controlled Thermonuclear Energy Research Program Annual Status report, LA-4585-MS (1970), p. 37.

14. A. Haberstich, Los Alamos Scientific Laboratory Controlled Thermonuclear Energy Research Program Annual Status report, LA-5250-PR (1972), p. 54.

15. Smithsonian Physical Tables, 9th edition, (1956) p. 393.

16. J. N. Di Marco and L. C. Burkhardt, Journ. Appl. Phys. 41, 3894 (1970).

17. LASL Controlled Thermonuclear Research Program Progress report, LA-5656-PR, (1973), p. 119.

18. R. A. Haarman and R. S. Dike, Meeting on Energy Storage, Compressions, and Switching, Torino, Italy, (November 1974), to be published.

19. L. C. Burkhardt, R. S. Dike, J. N. Di Marco, J. A. Phillips, R. A. Haarman, and A. E. Schofield, "The Magnetic Energy Storage System Used on ZT-1," ibid.

20. L. A. Artsimovich, S. V. Mirnov, V. S. Strelkov, Atomnaya Energiya 17, 3, 170 (1964).

21. V. S. Mukhovatov, Culham Meeting 2, 577 (1965).

22. Sinclair et al, Phys. Fluids 6, 937 (1963).

23. T. Jernigan and D. Meade, unpublished.

24. D. W. Kerst, A. A. Schupp, H. K. Forsen, J. of Nucl. Energy Pt. C, 5, 161, (1963).

25. Los Alamos Scientific Laboratory Controlled Thermonuclear Research Program Annual report, December 1973, p. 96.

26. W. Wolman and H. Kaden, Zeitschr. für techn. Physik 13, 330 (1932).

27. S. D. Winter, R. W. Kuenning, and G. G. Berg, UCRL preprint UCRL-71514, (1969).

28. R. S. Dike and R. W. Kewish, Jr., "The Development of a High-Explosive Driven Crowbar Switch," Proc. of the Fifth Symposium on Engineering Problems of Fusion Research, Princeton, N. J. (November 1973), IEEE, New York, p. 658.